Original Article

Experimental and numerical study of auxetic sandwich panels on 160 grams of PE4 blast loading

Faizal Arifurrahman[1,2] (iD),
Richard Critchley[1] and Ian Horsfall[1,3]

Abstract

Mines, specifically as Anti-Tank (AT) mines are a significant threat for defence vehicles. While approaches such as v-shaped hulls are currently used to deflect the blast products from such threats, such a solution is not always usable when hull standoff is limited. As such the development of a low profile, energy absorbing solution is desirable. One approach that has potential to achieve these requirements are sandwich panels. While sandwich panel cores can be constructed from various materials, one material of particular interest are auxetics. Auxetic are materials that exhibit a negative Poisson's ratio. This material has potential to be an efficient an impact energy absorber by increasing stiffness at local deformation by gathering mass at the impact location. This study investigates the effectiveness of novel auxetic core infills alongside three other panel types (monolithic, air gap, polymer foam sandwich) against buried charges. 160 grams of PE4 were buried in 100 mm depth and 500 mm stand off the target. Laser and High Speed Video (HSV) system were used to capture the deflection-time profile and load cell sensors were used to record the loading profile received by the panels. Experimental works were compared with numerical model. Explicit model were

[1]Survivability Lethality and Advanced Materials Group, Centre for Defence Engineering, Cranfield University, Defence Academy of the United Kingdom, Shrivenham, UK
[2]Lightweight Structures Research Group, Faculty of Mechanical and Aerospace Engineering, Institut Teknologi Bandung, Bandung, Indonesia
[3]RAL Space, STFC Rutherford Appleton Laboratory, Didcot, UK

Corresponding author:
Richard Critchley, Survivability Lethality and Advanced Materials Group, Centre for Defence Engineering, Cranfield University, Defence Academy of the United Kingdom, Shrivenham SN6 8LA, UK.
Email: r.critchley@cranfield.ac.uk

generated in LSDYNA software as 'initial impulse mine' keyword. The result found that the auxetic and foam core panels were effective in reducing peak structural loading and impulse by up to 33% and 34% respectively. Air-filled panels were the most effective to reduce the deflection of the rear of the plate, however variation between capture methods (HSV and Laser system) were reported, while numerical modelling provided comparable plate deflections responses. When normalised against panel weight, the air filled panels were experimentally the most efficient per unit mass system with the auxetics being the least effective.

Introduction

Anti-vehicle (AV) mines and Improvised Explosive Devices (IEDs) have become a feature of modern warfare. Since World War II, they have become the leading cause of vehicle loss [1]. AT mines with typically 6 kg of explosives can cause severe damage to the vehicle and injury or kill its occupants. Bird reported that 22% of the United States (U.S) military losses were due to landmines in World War II [2]. Furthermore, the percentage of fatality in the Korean War, Vietnam War, Persian Gulf operation, and Somalia were 55%, 70%, 59%, and 60%, respectively. NATO (North Atlantic Treaty Organisation) presented the data of the AV mine data in its technical report [3]. The data shows the number of incidents resulting in casualties and fatalities between the years 1998 to 2006. The quantity of accidents and casualties depended on the year and the conflict. The number of incidents increased during such disputes, such as the former Yugoslavia, Afghanistan, and Iraq conflict. During this period, there were approximately 255 casualties and 235 fatalities on more than 190 AV mine incidents all over the world. In a recent conflict, U.S overseas contingency operation of Iraq and Afghanistan, AT mines and IEDs were responsible for nearly half of total 4,153 US troops deaths since 2006 [4].

As IEDs and AT mines continue to improve, so must the protection. The mitigation methods have changed with vehicle generation by designing the improved anti-land mine structures [5]. Whilst rolled homogeneous armour is traditionally used as vehicle armour, it is unsuitable in mass terms to merely increase thickness to protect against larger or more sophisticated mine threats. As such, various alternative approaches have been investigated, including structural alterations, sacrificial plates, the use of energy absorbing materials and alternative materials [5–7].

However, one material yet to gain traction for vehicle mine protection are auxetics. Auxetics are a modern class of materials that have demonstrated Improved mechanical properties such as fracture toughness [8–10], resilience [11], shear resistance [12–16], or even vibration response [17–19] owing to their negative Poisson's ratio [20]. The negative Poisson's ratio causes the material thicker when stretched or will shrink towards the centre of compression loading. The shrinkage area becomes denser to increase indentation resistance [21–23]. To date a wide range of materials have been modified to be auxetic including polymers [24], metals [12,25], ceramics [26–28], composites [29,30], and fibres [31,32]. In nature, these materials can be found in black phosphorus [33] or biological tissues [34]. Since their inception, several applications for the defence field have been proposed. In the defence field, auxetics has an opportunity as a shield or barrier by absorbing the impact energy [35–37]. The density enhancement of auxetic makes it possible to take in the explosion shock energy and reduce the barrier damage. The progressive crushing of auxetic core results in densification and concentration of material in the centre. The densification absorbs the impact load and reduce the back-face deflection [38]. More recently the concept of using auxetic materials as an energy absorber in blast impact mitigation have been explored [39,40].

The idea of using a core sandwich material as a blast protector is not new. Several numerical and analytical studies of sandwich structure responses subjected to impulse loading have been conducted [40–46]. The studies have varied materials, panel thickness, or panel configuration. In the earlier work, Schenk et al. [42] explored the stacked folded material core for sandwich configuration. Numerical modelling on quasi-static and dynamic loading has been executed to find the optimum core architecture for maximum for blast mitigation. Imbalzano conducted the numerical analysis of auxetic composite under blast loading [41]. The curvature or chiral form also been investigated to understand how the modified auxetic geometry effects their mechanical properties [37]. The experimental investigation of the blast impact on the monolithic panel structures have been done [47–49]. However, only a few studies have been undertaken using explosive loading due to the potential factors including cost, and accessibility. Moreover, the buried explosive loading is also a rare study until present. Specifically for auxetic materials, Qi et al. [39] compared the numerical and experimental results of sandwich panels under 250 grams of composition B explosive. They examined the areal specific energy absorption (ASEA), and the study indicated the potential of auxetic in the protection of civil and vehicle objects. Moreover, several numerical methods were compared to experimental explosive loading [50]. For the cellular sandwich panel, Holloman et al. [51] investigated the impulse transfer of sand impact, one key observation is that the strong core cellular structures transferred the same impulse as a solid block while the softer core transferred less impulse.

Furthermore, the mine explosion phenomenon shows that the short duration of explosion in comparison to the natural period of the vehicle structure makes the pressure-time loading is not relevant [52,53]. Otherwise, the total impulse of blast

impact is a critical indicator of blast effect on the vehicle structure. This indicator can be approximated from the Tremblay equation [54]. Deflection is one of the parameters to measure the damage on the structure and how far mine explosion able to deflect the vehicle structure. Therefore, the objectives of this study are: (i) to conduct the explosion testing of 160 grams of PE-4 explosives, which is relatively larger amount of size than the existed works, buried under the fine building sand (ii) to replicate the observed testing in numerical modelling; (iii) to compare the results between the experimental and numerical simulation; and (iv) to investigate the displacement and impulse response on four different panel configurations, i.e. monolithic, air gap, Styrofoam core and steel-made auxetic sandwich. In addition, the specific energy absorption will be presented to figure out the effectiveness of auxetic structures in absorbing impulse damage.

Finite element modelling

Computational modelling was undertaken using LS-DYNA pre post V4.5 with the explicit solver of R910 double-precision, using a 64 bit Windows 7, 32 GB RAM, i7 2.6 GHz 8 core processor computer. This is an an explicit non-linear dynamic finite element code which is appropriate for handling the dynamics testing and complex contact interaction between the structure sheets. . The steel panels were fully modelled using a Belytschko-Lin-Tsay four-node thin shell element type, due to the simple and reliable shell element [55]. Element size was determined through the mesh convergence test detailed below.

Mesh convergence test

Mesh convergence is required to obtain the optimum element size by considering numerical accuracy and simulation solve time. Several number of 'impulse mine' simulations were carried out to determine the appropriate shell element size. Shell element size of 8 mm, 6 mm, 5 mm, 4 mm, and 2.5 mm of auxetic sandwich panels were modelled to investigate the central node displacement and the effects of resolution on the simulation output, as shown in the Figure 1. It indicated that the shell element size affects the modelling result. The use of 8 mm and 6 mm that have a bigger element size than 5 mm and 4 mm produced a higher deflection. 5 and 4 mm element size model is shown to be converged to the value of 12.4 mm. We also considered the running memory allocation to choose the proper element size. Memory allocation is required to process the modelling. Higher number of elements would demand higher memory requirement. Figure 1 indicated that reducing 1 mm size would increase the memory requirement by factor of 2. The running time of these simulations were not the issue because as presented in Figure 1 that the maximum CPU time for 4 mm running element size was only 812 s. The running time was increasing when the element size was reduced. By reducing the element size by 1 mm, the running time of auxetic panel was increasing to 1.1 to 3.6 times and the required memory to finish the job was increasing
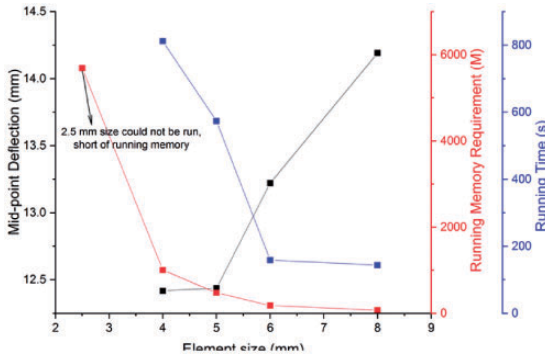
Figure 1. Mesh convergence test detailing relationship between element size, maximum deflection and memory requirement.

more than double. Moreover, especially for sandwich structure that requires complex interaction between the layer and numerous elements, thin metal shell element or foam solid element smaller than 5 mm will result in higher computational times. Due to the relatively smaller difference in deflection for smaller elements, the authors deemed the extra computational time unnecessary.

Buried charge modelling

We considered that 'Initial impulse mine' were suitable in this case due to the accuracy and considered less time consuming than other methods [56]. The buried charge was simulated using 'initial impulse mine' keyword [57], and was defined in terms of TNT equivalence; 160 gram mass of PE4 explosive is equivalent to 208 gram of TNT. This rule follows Bogosian et al. study [58]. The 'initial impulse mine' function was derived based on Tremblay equation [54]. Figure 2 shows the 'initial impulse mine' keyword conditions which is replicates the Tremblay model. Tremblay modified the empirical equation of specific impulse (impulse per unit area) presented by Westine et al. [59]. By integrating the specific impulse, the total impulse was acquired. The equation below determines the total impulse for a quadrangular deflector panel above the land mine

$$i_v = k_0(S_1 + S_2)\left(1 + \frac{7\delta}{9z}\right)\sqrt{\frac{\rho E}{z}} \tag{1}$$

where k_0 is a constant, S_1 and S_2 are variables of the error function. These variables determine the approximation accuracy to calculate the total impulse. Tremblay also set the non-dimensional parameters of Westine et al. model concerning the charge position range as presented in Table 1, where δ is depth of burial charge in [m], E is energy released by explosive charge in [J], A is cross-sectional area of mine in [m^3], ρ is soil density in [kg/m^3], c is the seismic P-wave
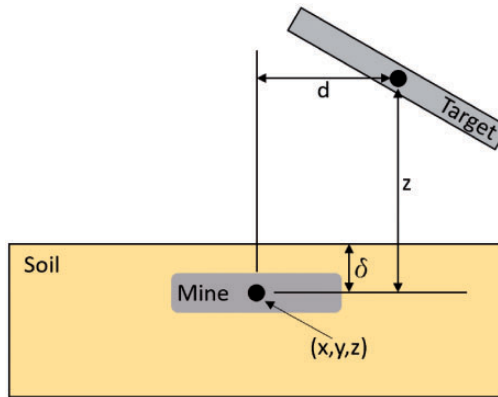
Figure 2. 'Initial Impulse Mine' model where the explosive charge was modelled as point of charge relative to the depth of burial, standoff distance, and soil density; adapted from [54].

Table 1. Tremblay's non-dimensional parameters [54].

	Model parameter	
$0.106 \leq$	$\frac{\delta}{z} = 0.2$	≤ 1.0
$6.35 \leq$	$\frac{E/A}{\rho c^2 z} = 5.12$	≤ 150
$0.154 \leq$	$\frac{\sqrt{A}}{z} = 0.102$	≤ 4.48
$0 \leq$	$\frac{d}{z} = 0.4$	≤ 19.3

velocity in the soil in [m/s], and z is standoff distance of the point of charge to the centre of mine in [m].

Another limitation is a factor 1.8 to the empirical specific impulse. The predicted impulse occurred is between the interval of $i_v/1.8$ to $1.8i_v$. This expected impulse is also in agreement with William et al. study that determined 66% correction factor to produce a good correlation with experimental observations [60].

Boundary conditions

The boundary condition at the panel edges were set to be fixed and simulated the clamped joint at the edge of the testing panel. Fix joint restrained the panel to move in six degrees of freedoms, three degrees of translational and three degrees of rotational.

Contact in the sandwich panels was required for air gap, foam, and auxetic core. 'Automatic surface to surface' contact was applied to those configurations. It defined the contact between the elements of panel and core as a friction contact. This contact type provided the same model according to the real condition where the metal sheet only touched in the core without any adhesion or bonding. Also,
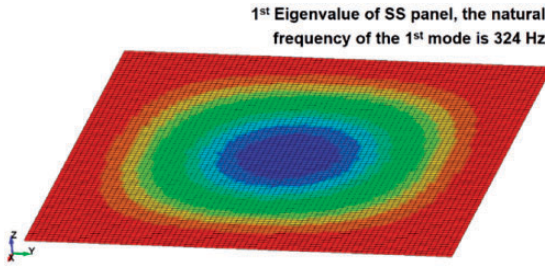
Figure 3. Single steel panel simulated by modal analysis to calculate natural frequency and appropriate dampening ratio.

'automatic single surface' was also defined to the panel surfaces to prevent the interpenetration between each contacting elements during the deformation.

Damping response also must be considered to obtain the precise structure response. The result of energy dissipation forms damping during structural vibration, which is affected by structural damping (material itself) and Colomb damping on the dry surface of the clamped joint. The conservation approach neglects this interaction between the charge source in a shock wave and the structure [61]. In this study, dissipated energy due to the plastic deformation is far greater than the damping energy. However, other studies show that the damping ratio can overestimate the deflections for lighter structure in low-level blast loads [62]. The effect of the damping ratio has a considered effect on the displacement response [19,63–65]. We have roughly calculated to predict the damping ratio from the overshoot of displacement trace of monolithic panels. The results indicated that the damping ratio ranged between 5–11%. So in this study, the damping ratio coefficient in numerical will be assumed as 5% of critical damping. Figure 3 displays the first mode or critical mode of the monolithic panel occurs at 324 Hz.

Material model

The steel material was modelled as an elasto-plastic material with kinematic hardening. The steel panel was modelled using a plastic kinematic material model that ignored the effect of thermal changes due to the limitation of material data [55]. This model is also used by Jin to model his plate [43]. A plastic kinematic model is acceptable since the lack of stress-strain data. This material model also includes the damage criterion when the failure stress reached. The numerical model included strain rate effects in the model as Cowper Symonds constants of mild steel [66,67]. These constants are applied to the surface panels and auxetics core. Next, the foam material was created as a crushable foam with isotropic properties [68,69]. For crushable foam, strain-stress data was generated by inputting the plasticity points. The foam element is deleted when the strain reaches the failure criterion of elongation at break. The mechanical properties of the utilized mild steel and

Styrofoam material were taken from the ASTM material database [70] and technical data from Wickes Ltd. [71], as shown in Table 2.

Experimental work

Buried charges

Twelve tests were conducted across four different panel configurations at a fixed standoff distance of 400 mm from the sand surface. A spherical charge of 160 gram PE-4 was buried at a depth of 100 mm, from the centre to the ground surface in the sand, supplied by Wickes, UK (Figure 4). The sand was naturally dried within a laboratory environment for a minimum of seven days and raked twice daily to facilitate uniform drying. Prior to the testing, the sand humidity was recorded using a WT Meter at five different locations, four on the surface, and one at the base, where the charge was placed. A summary of the humidity readings and taken test days are given in Appendix 1.

Table 2. Steel and foam material properties.

BS1449 CR4 steel properties		Styrofoam by Craftfoam blue	
Density (kg/m^3)	7830.0	Density (kg/m^3)	33.0
Elastic Modulus (GPa)	200	Elastic Modulus (kPa)	24
Poisson's ratio	0.29	Poisson's ratio	0.20
Yield strength (MPa)	280	Compressive strength (kPa)	50
Failure strain (%)	28		
Cowper Symonds parameter, D (s^{-1})	40		
Cowper Symonds parameter, q	5		

Figure 4. Contained sand with centre location excavated to enable placement of PE4.

Material and panel specifications

A series of test panels, dimensions 500 mm × 500 mm were manufactured at Cranfield University workshops, as described in Table 3. The flat steel plates were 6 mm in thickness, while the sandwich panels comprised of four components; 2 × 3 mm steel plates, a support frame, and a core. The support frame was manufactured from C-Bar and had external dimensions 500 mm × 500 mm × 50 mm, with interior dimensions of 400 mm × 400 mm, as illustrated in Figure 5. A series of M10 bolt fasteners were placed at regular intervals of distance 112.5 mm, to facilitate the fixing of the plates to the support frame and the experimental test rig.

Three different core materials were investigated: Atmospheric air (air gap), Craftfoam Blue, and an auxetic re-entrant structure. Craftfoam Blue, supplied by PanelSystems [72], is a low-density Polystyrene Foam typically used for model making and prototyping. Metal sheets were supplied of dimensions 600 mm × 600 mm × 50 mm, and cut down to 400 mm × 400 mm × 50 mm using a band saw. The auxetic core was manufactured using a bending method from 1 mm sheet mild steel to a re-entrant bowtie structure (Figure 6). Due to the limitation of bending tools, the 400 mm × 400 mm auxetic core was manufactured as two 200 mm × 400 mm parts and welded to form a single core. Welding was used to join the closed side and each bow tie pieces to create the configuration.

Data acquisitions

Experiments were undertaken on the Explosive Range and Demonstration Area (ERDA) located at the Shrivenham campus of Cranfield University, over a three-day period. A custom-built support rig fixed the panels, which provide rigid sample support that contain the explosives under the sample (Figure 7). The support rig consists of three main components i.e., explosive plates, I-Beam cross sections,

Table 3. Testing panel configurations used within this study.

| Test number	Testing code	Configuration	Layer thickness (mm), in sequence
1	SS1	Single steel plate	6
2	SS2	Single steel plate	6
3	SS3	Single steel plate	6
4	SA1	Steel - Air gap - Steel	3 - 50 - 3
5	SA2	Steel - Air gap - Steel	3 - 50 - 3
6	SA3	Steel - Air gap - Steel	3 - 50 - 3
7	SF1	Steel - Styrofoam - Steel	3 - 50 - 3
8	SF2	Steel - Styrofoam - Steel	3 - 50 - 3
9	SF3	Steel - Styrofoam - Steel	3 - 50 - 3
10	SX1	Steel - Auxetic core - Steel	3 - 50 - 3
11	SX2	Steel - Auxetic core - Steel	3 - 50 - 3
12	SX3	Steel - Auxetic core - Steel	3 - 50 - 3
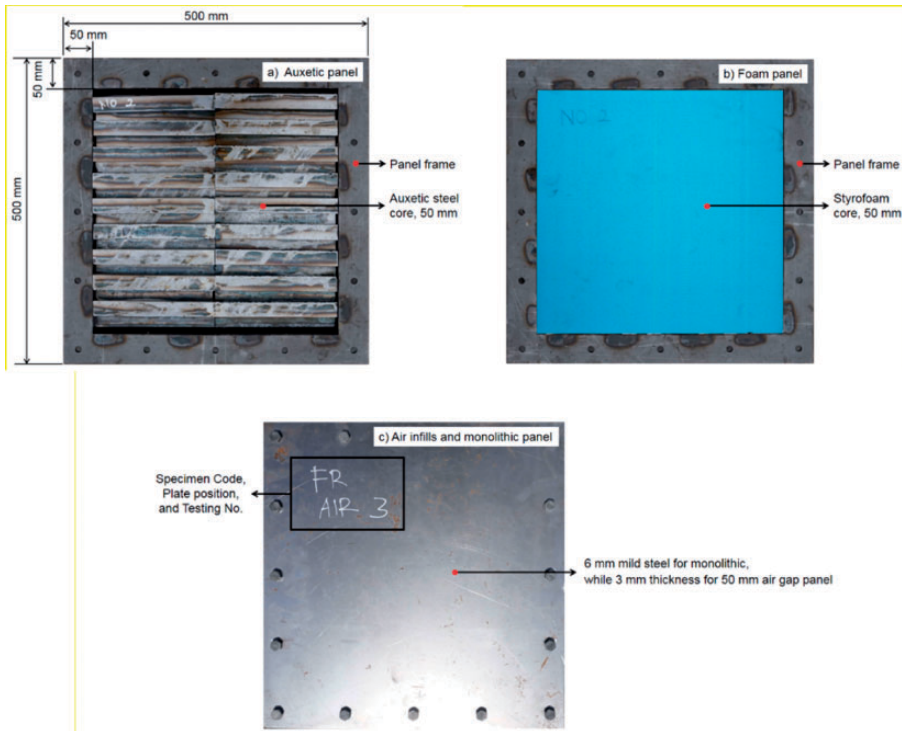
Figure 5. Panel geometry has dimension of 500 mm x 500 mm mild steel panel with the frame width of 50 mm at each edge constraint the sample. The effective area of exploded panel is 400 mm x 400 mm. (a) Auxetic sandwich panel; (b) Foam infills panel; (c) Air infills and monolithic panel.

and frames. The plates were attached to the blast rig by anchoring the corners to the underbelly of the I-beams and sandwiched between two thick pieces of square steel at the top. Located between the plates and test rig at opposite corners were two Piezo-electric Kistler sensors (9061 A 0–200 kN). Load cells took the loading data by changing the deformation of compressed cells during the explosion to the voltage signal. The acquisition data convert the voltage response in the load cells to the Newton unit. Data was captured at a sampling rate of 100 kHz using a Prosig 8012 acquisition system coupled with a charge amplifier. A pre-trigger (triggered above 30 kN) set at 0.1 s was used to ensure event capture. A calibrated hammer equipped with a load cell was used to validate the load cells.

Plate deflection was measured using two methods: a Keyence LK G507 displacement laser sensor and a high speed Phantom V12 camera. The laser sensor was position centrally above the test panel and had a set working range set at 0 to 100 mm, over a 10 V range. Data were sampled at 10 kHz and triggered by the piezo-electric pre-trigger. The laser signal instrument was installed on the blast rig
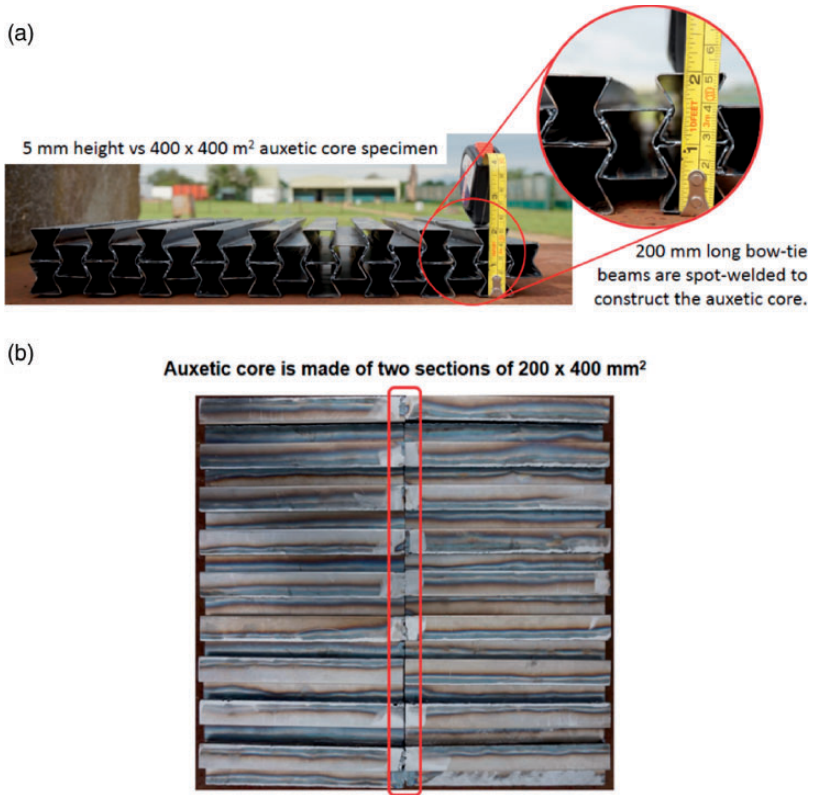
(a)

5 mm height vs 400 x 400 m² auxetic core specimen

200 mm long bow-tie beams are spot-welded to construct the auxetic core.

(b)

Auxetic core is made of two sections of 200 x 400 mm²

Figure 6. An example of the re-entrant auxetic core in (a) side on and (b) a top down view.

1. i-beam cross sections part, to attach the specimens

2. Frames, to build the blast rig structures

3. Bucket shield, to cover the sand splash during the explosion

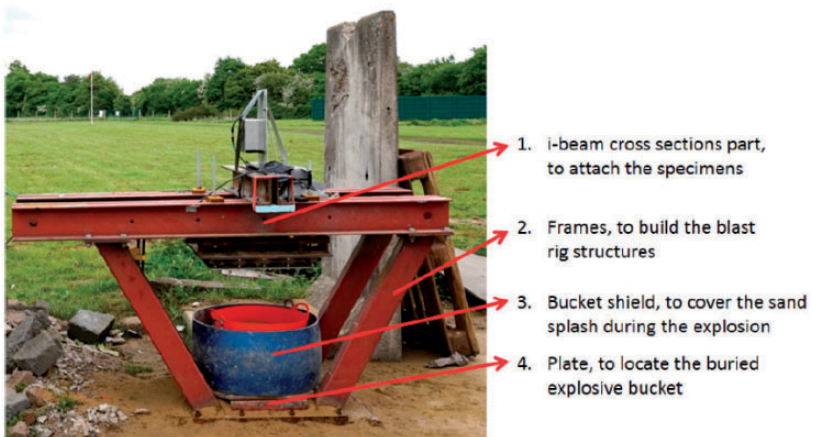4. Plate, to locate the buried explosive bucket

Figure 7. Instrumented blast rig instrument setup at the ERDA.

perpendicularly at the middle point of the panel. The deflection was measured by pointing the laser signal and measuring the change of the laser length. Raw data from the laser signal was processed using point data average method to remove the noise as normalized data.

The High Speed Video (HSV) captured using Phantom V12 camera was located at a distance behind a Pendine block barricade and used a mirror to observe the plate surface at a 540×540 pixel resolution at 21,005 FPS (Figure 8(a)). The angle of incidence of the mirror reflection was corrected using the trigonometric relationship. A simple trigonometry concept determined the vertical plate displacement, where theta (θ) was measured to be 34°. For a high-speed camera, due to the perspective view change on the image, the horizontal distance of the white points was used. On the back face of the panels, white spots were marked in a 3×3 grid, spaced 50 mm apart to enable post-experimental displacement tracking using the Phantom Camera Control software (PCC) 2.6. The laser signal was directly aimed at the middle white spot (Figure 8(b)). As part of the tracking process, the PCC
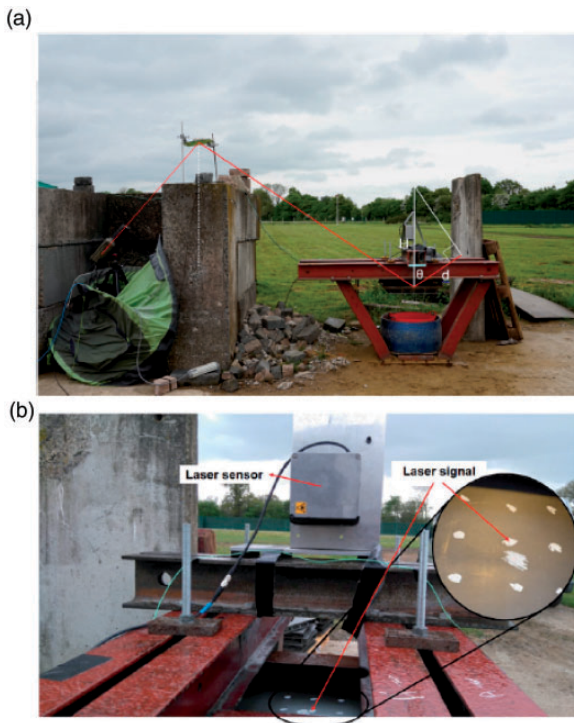

Figure 8. (a) Phantom V12 high-speed camera installation to record the central displacement of the panel. The camera captured by reflected the response by the mirror with theta, θ is 34°; (b) The 5 mm apart white spots in 3 x 3 grid is used for V12 high speed camera processing through the PCC software to trace the displacement.

software requires a scale calibration to relate pixels to distance. For each video, scale calibration was taken about the horizontal axis, and measured between the centres of two 50 mm apart marks. Once calibrated, a tracking region was set. In all tests, the tracking region was set about the central mark as it remained within view until the detonation products and sand obscured the plate. A comprehensive method of how tracking works within PCC is detailed in [73]. Plate deflection measured using the Keyence LK G507 was measured centrally, and zeroed before each test to mitigate against pre-loading.

Result and discussion

Negative Poisson's ratio behaviour

The auxetic core was compressed computationally to determine the bulk Poisson's ratio as a structural characteristic prior to experimental testing (Figure 9), where the greatest negative Poisson's ratio (–0.35) was shown to occur at the beginning of compression. At the initial condition, the cross-section of the auxetic panel is shown as a bow-tie structure in perfect shape without welding condition between the cellular walls. This shell element modelling was different from the real condition where the point welding used to join the bow-tie cellular. At 0.20 strain condition, the shrinkage arrangement to the centre direction started to appear. Next on 0.65 strain, the core panel became fully dense in the central region before it expanded and regained to the base material Poisson's ratio on 0.74 strain.

Impulse and blast loading

Figure 10 shows the average peak force-time profiles for the different panel configurations, with a summary of individual data given in Table 4. To mitigate experimental noise, a 5-point rolling average filter was applied to the raw force data.

All experiments exhibited comparable force-time profiles, where a primary peak loading lasting between 2 to 3 ms in duration before transitioning to a negative load. As time progresses, a series of positive and negative peaks repeat until full
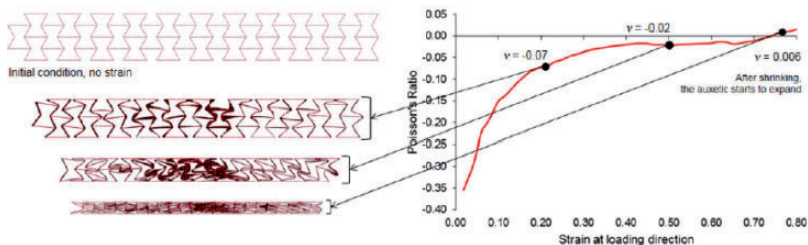

Figure 9. Compression modelling of the auxetic core with structural bulk Poisson's ratio detailed graphically relative to strain.
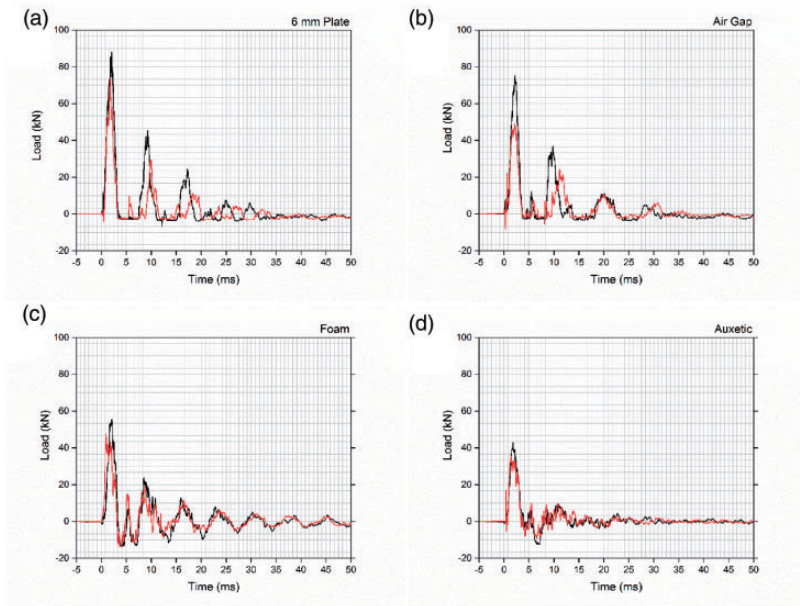
Figure 10. Force-time profiles for (a) 6 mm Plate, (b) Air Filled Panels, (c) Foam filled Panels, and (d) auxetic filled panels, for sensors S/N 389 (——) and S/N 625 (——).

Table 4. Experimental and numerical results of mean load and central transversal displacement.

Configuration	Experimental sample	Average load, S/N 389 (kN)	Average load, S/N 625 (kN)	Total impulse (kN.s)	Z displacement (back plate)			Z Displacement (face plate) (mm)
					Laser (mm)	Video (mm)	Model (mm)	
Monolithic	SS1	–	–	–	10.91	11.70	17.44	–
	SS2	–	–	–	13.33	9.84		
	SS3	–	–	–	25.32	14.72		
	SS4	84.47	67.84	494	14.19	13.98		
Air gap	SA1	57.21	–	–	–	10.78	15.64	48.78
	SA2	53.53	43.36	166	18.36	10.68		
	SA3	73.75	47.26	393	8.38	13.26		
Styrofoam core	SF1	59.35	46.25	302	25.67	–	7.3	53.1
	SF2	59.83	38.14	297	2.45	-		
	SF3	54.60	44.01	335	22.28	15.26		
Auxetic core	SX1	41.16	39.54	262	-	13.45	12.44	3.67
	SX2	41.58	34.82	246	20.87	–		
	SX3	66.34	55.94	251	16.68	–		
	SX4	66.34	55.94	257	13.16	10.46		

attenuation. The 6 mm plate data was the exception as no discernible negative loading data is shown. The absence of negative loading, suggests that either the DAQ system is cutting off data, or sensors were not fixed correctly. Unfortunately, it is difficult to clarify this, as unlike the other profiles, only the data from the 6 mm plate test 4 is presented in Figure 10, as DAQ failure resulted in no usable data being recorded due to an over-ranging error. To ensure this behaviour did not occur in later tests a 10:1 channel reducer was introduced.

Good correlation existed between the two sensors with the exception of the air-filled plates which were particularly noisy. In most tests greater loading was experienced by sensor S/N 389, indicating an irregular loading pattern. There are two potential sources for the irregular loading. One reason could be due to support plate distortion induced from repeated exposure to the blast. This explanation however fails to account for the lack of consistency throughout testing. A more likely explanation is the soil ejecta impacting the plate is either anisotropic in impact location or in geometrical shape. For mediums such as the sand, the loading at any discrete location is dictated by the particle size that impacts the location and its momentum induced from the explosive charge [58]. This coupled with the variation in sand humidity (detailed in Appendix 1) makes for a more likely explanation. Unfortunately due to the location of the high speed camera coupled with the blast products, the ability to observe loading pattern from the ejecta was not observable within this study.

On average the monolithic samples exhibited the greatest peak loading of 84.47 kN, with auxetic samples exhibiting the lowest at 41.16 kN. Generally, all panels were highly variable in similar range, with error variance being approximately 14% for S/N 389 and 11% for S/N 625. Greater consistency was shown for the foam cored panels with error variance approximately 3% and 4% of the mean for S/N 389 and S/N 625 sensors respectively. Assuming the 6 mm plate as the control, both the auxetic and foam infills offer a mean loading and impulse mitigation of 33% and 34% respectively. Alternatively, the air filled panels have the potential to both amplify and mitigate the pressure and impulse experienced.

In a series of tests a low intensity, rapid loading event occurred prior to first peak without bias across panel configurations. Such behaviour has been previously reported by Ramasamy et al. [74], and is referred to as the detached shock wave. While this interaction induces a loading effect on the plate, due to acoustic impedance between the sand and air, only a small fraction of the incident shock is transmitted into the air, causing the resultant air shock to have minimal influence on the target structure [75]. Instead, the initial peak loading is caused by the soil ejecta. According to Deshpande et al. [76] and Børvik [77] up to two thirds of the impulse is delivered to a vehicle is from the soil ejecta, with the remaining third delivered by the blast products.

While the fixed conditions of testing coupled with the test data, can allow for the assumption that they are induced by the blast products and soil ejecta, it fails to account for the irregular subsequent data peaks trends such as, the third peaks always being lower than the fourth. It is postulated that this behaviour could be

caused by the presence of a reflected wave between the rig and the panel during the loading event. Alternatively, it could be caused by the fluttering or vibration response of the structure induced from the blast impact. The flutter occurred in an oscillation trend between the peaks. Frequencies were calculated from the period between the peaks and were found to be approximately 1282 Hz, 1338 Hz, 1000 Hz, 1420 Hz, for monolithic, air gap, foam, and auxetic respectively. We compared with the numerical analysis and found out that the 6th mode of monolithic damped frequency is 1194 Hz. The numerical result strengthens the argument that it could be a damped oscillation. It is consistent also with dynamics principles where stiffer the panel, higher the frequency mode would be.

When considered in the impulse domain the auxetic panels exhibited the lowest mean impulse while the monolithics exhibited the most (Figure 11). The single 6 mm plates were comparable to the air plates in measured impulse, while the foam infills were more comparable to the auxetic panels. Once again the air-filled panels were highly variable with error variance being approximately 57.43% of the mean, while foam and auxetic panel configurations were fairly consistent with an average error of 6.63% and 2.75% of the mean respectively. Although unclear why the air-filled panels demonstrated such large variation, it is suspected that it is caused by the high pressure experienced at sensor S/N 39 in test SA3. Although the cause of this high pressure is difficult to ascertain, the variance indicates that the soil ejecta that interacts with the plate is either anisotropic in impact location or in geometrical shape. For mediums such as the sand used in this study, the experienced loading at any discrete location is dictated by the particle size at that location and its momentum induced from the explosive charge [78]. This is further supported by the wider literature where soil type and charge shape are reported to be the principle parameters that influence loading [75,79–85].
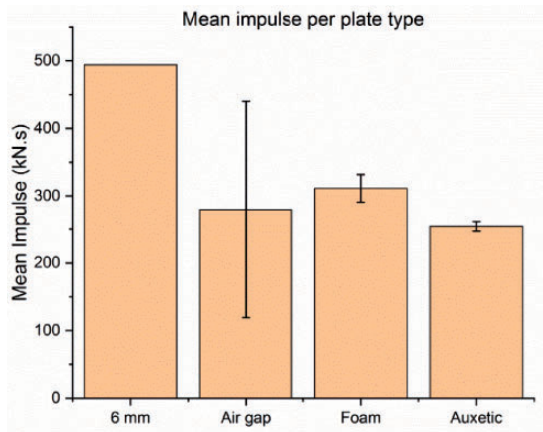

Figure 11. Mean impulse per panel type where errors represent standard deviation.

As such if some part of the soil ejecta impacted directly at the sensor location, a greater loading and subsequent impulse would be recorded. Unfortunately with only two data points (both significantly different), it is difficult to validate this theory.

In this study, the non-dimensional parameters did not fulfil the requirements. All variables were input in the equation and compared both results of total impulse in the MATLAB and LS-DYNA. Both the MATLAB and LS-DYNA models yielded comparable results of 649 and 650 kN.s, respectively. Even though the 15% reduction is a range between the intervals of 1.8 factor, this reduction is caused by the non-fulfilment of the parameter limitations required. However, by scaling down the total impulse in LS-DYNA, the numerical results were expected to show similar deflection compared to the experimental observation.

By scaling down the total impulse in the simulation setup, the simulation showed expected results with similar deflection compared to the experimental observation, as shown in the next sub-section. The mean impulse for all panels, excluding 6 mm was approximately 300 kN.s. Solving Tremblay to calculate the vertical impulse of buried mine [54] using the experimental parameters herein, an impulse of 650 kN.s was produced; a value significantly different than the observed result. It is suspected that the deviation between experimental and calculated value as the parameter criteria did not fulfil the Tremblay function limitation, as detailed in Table 1. In light of this, the mean impulse value for each panel configuration was used in the numerical analysis by scaling the impulse to replicate the actual deflection response.

Deflection response

Figure 12 shows an example of deflection-time profiles recorded by the laser. Noise was removed 5-point rolling average filter and normalized about the zero. Mean maximum deflection data the laser system and HSV is provided in Figure 13.

The air filled panels exhibited the lowest displacement, followed by the 6 mm, foam, and auxetic respectively. Similarly the laser system, HSV indicated that the lowest mean displacement was exhibited by the air panels, followed by auxetic, 6 mm, and foam infills respectively.

All instances, HSV recorded consistently a smaller displacement than the laser by up to 29%. Both systems were considerably variable with error (given by standard deviation) ranging from 23% to 75% and 10% to 17% of the mean displacement for the laser system and HVS respectively. The maximum deflection occurs at the interval between 0.5 – 1 ms on all panels. Both systems were relatively comparable with mean deflections recorded between 13 mm to 27 mm, and 11 mm to 15 mm being recorded for the laser system and HSV respectively.

Analysis of the temporal dominion found that displacement occurred between a mean duration of 2.0 ± 0.6 ms and 3.6 ± 0.65 ms for the laser system and HSV, respectively (Figure 14). Interestingly, the laser system showed that as the panels went from a single panel, to a more composite panel, the displacement duration
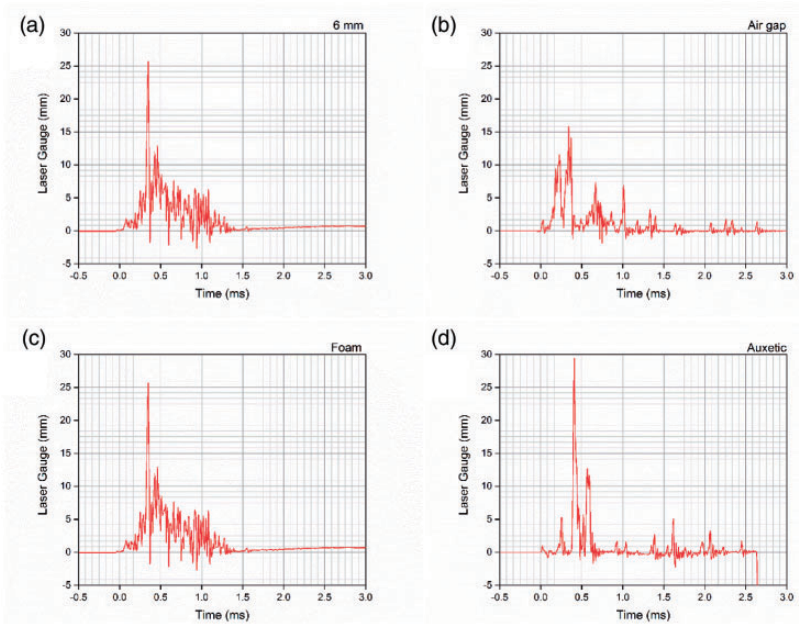
Figure 12. Deflection-time profile based on the laser signal result for (a) 6 mm Plate, (b) Air Filled Panels, (c) Foam filled Panels and (d) auxetic filled panels.
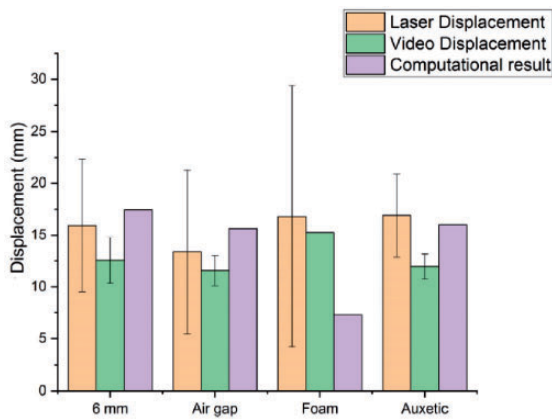

Figure 13. Mid-point displacement of the panels: experimental vs numerical result. Laser system provides physical location measurement (panel displacement) during testing to provide comparison to secondary measurement from HSV and provide validation to computational model.
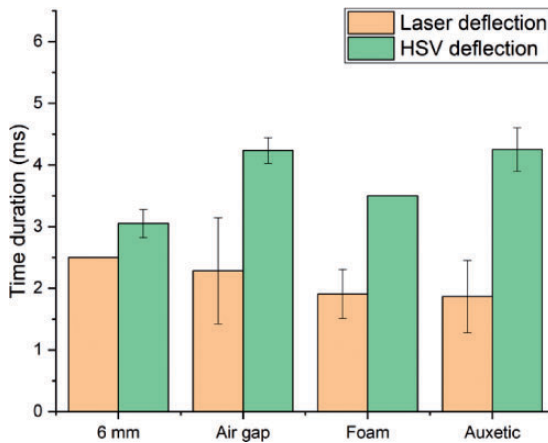
Figure 14. Time duration of displacement per panel type using laser system and HSV.

decreased, with the auxetic panels being the lowest. Alternatively, the HSV presents that changing from a single plate to a composite panel the displacement duration either increases (air filled and auxetic core) or remains comparable.

Interestingly stand deviation between panels was also shown to be influenced by measurement technique. The laser system reported a more broad range of variance from 8% to 32%, while the video had a variance of 1% to 3% of the mean displacement mean duration respectively. The differences between measured displacements are likely due to a number of factors, the most influence being location of the sensing system. In the case of the HSV, the camera was protected from the majority of the blast effects by the Pendine wall allowing for a continued observation of the event. While interactions of the blast products on the mirror are likely to play a role, the low error between datasets suggests that its influence is likely minimal. On the contrary, the laser system was directly located above the panel system and was more subjected to the blast products, as evident by the many dislocation of the laser system post explosive tests. Data capture rate is also likely to play a role in the fidelity of the data, however the influence of such factor is not considered herein.

When compared against the models (Figure 13 and Table 4), the difference between maximum model deflections and the mean panel deflections recorded by laser system and the HSV were -56% to 16% and -52% to 38% respectively, with the biggest deviation exhibited by the foam filled panels. These deviations are likely caused by a coupling of idealised conditions induced through computer modelling along with assumptions and simplifications made within material modelling. For example instead of developing the smooth negative exponential of stress-strain function, a plastic kinematic material model was used which only generates a trapezoidal function [55]. This simplification may also account large deviation observed between the foam experimental and numerical results. Unlike in the

experimental where the foam would be compressed and compact until densification, the model did not replicate the densification effect.

During the densification, the modulus is drastically changed from the sloping plateau to the steep second modulus. However, in the numerical, the foam material absorbed the impact energy by shrinking the element. This stage worked in stress plateau region. After that, the second modulus is input similarly with the first elastic modulus due to the lack of true stress-strain data. It contributes to reduce the deflection of back plate because we assume that the foam core would still absorb the energy in densification region, instead of loading the back plate. It is also suspected that the application of using a deletion mechanism on the foam element when it has reached the failure stress due to the pressure traveling from the face plate, where in reality the foam would continue to load the back plate.

A notable deviation was also observed for the auxetic panel where it was found that 160 grams of PE4 failed to initiate re-entrant behaviour to absorb the energy, although some transversal deflection did occur (Figure 15). Without being able to observe the auxetic core loading and deflection during the explosive event, it is difficult to confirm if this behaviour was isolated to the model or indicative of real world behaviour. Interestingly post impact there was evident of damage to the auxetic core in the way spot weld failure between the auxetic cells (Figure 16), and is likely one of the principle mechanisms of blast load absorption. This behaviour failed to be replicated in the auxetic model as the spot welding was not modelled, and thus could influence the model response as it did not have natural failure locations.

The auxetic model also saw the back plate deflect further than the face plate due to several possibilities. The absence of adhesive between each plate could oscillate each layer during the explosion and also the mechanism of absorption of explosive energy that could be mistaken. We assume that the stiffness of the same thickness face plate and back plate is the cause. The 3 mm panel configuration on the top and bottom behaves like a solid structure and only transfer the loading from the front to the bottom. Whereas the face plate should have been the first side to be hit by
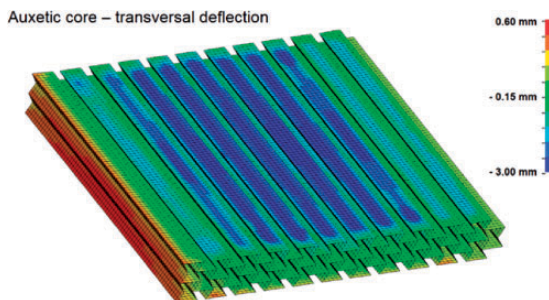

Figure 15. The transversal deflection profile of auxetic core at 0.9 ms. The face part shows the higher deflection due to the first momentum transfer directly from the face plate.

the sand ejecta, then the loading was transferred to the core so that the auxetic shrink. This shrinkage behaviour should be an absorbent of impact energy so that deflection can be reduced at the back of the plate. This result may be different if the back plate that is on the inside has a thicker size or vice versa, the face plate is thinner.

Other notable damage to occur throughout testing was the presence of denting on the front panels (Figure 17). While every effort was taken to ensure the sand was levelled prior to testing, the spread of denting indicates that either the soil ejecta didn't load uniformly or that clumping occurred. This non uniform loading could explain the variance in each panel configuration as shown in Table 4.
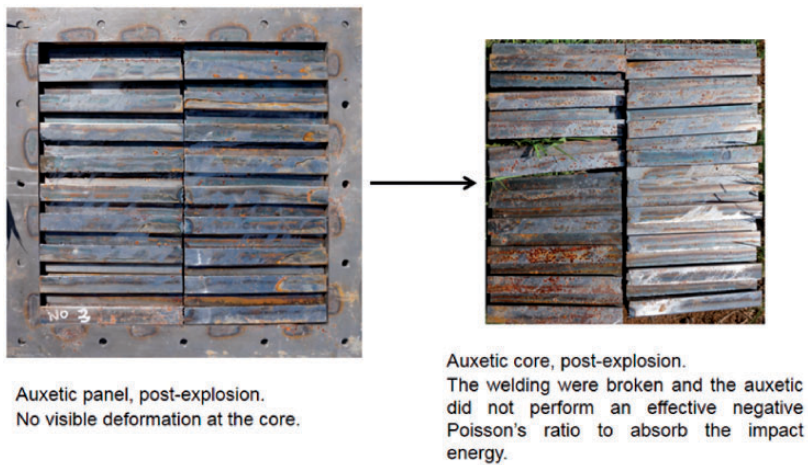

Auxetic panel, post-explosion.
No visible deformation at the core.

Auxetic core, post-explosion.
The welding were broken and the auxetic did not perform an effective negative Poisson's ratio to absorb the impact energy.

Figure 16. Auxetic sandwich panel post-test condition highlighting weld failure and compression of the lattice structure.

(a)

Even after sifted the sand before used, the lump sand were found at some local points

(b)

Dents were found in the air gap panels (face plate).
It is confirmed that the face section was plastic deformed.
Moreover, the dents showed that the sand ejecta was not uniform
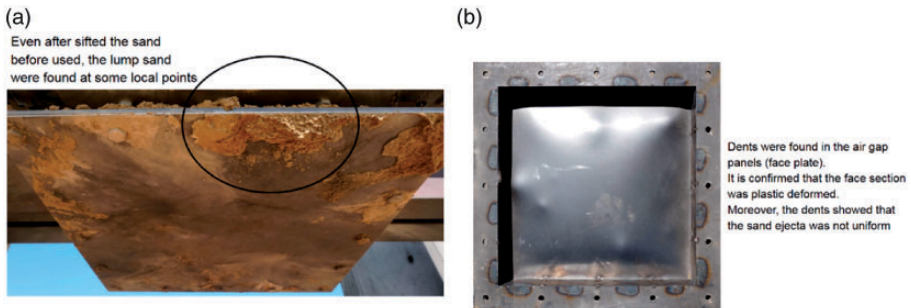
Figure 17. Dent damage observed on (a) front panel for monolithic and air gap panels, highlighting potential non-uniform sand ejecta, and (b) rear panel.
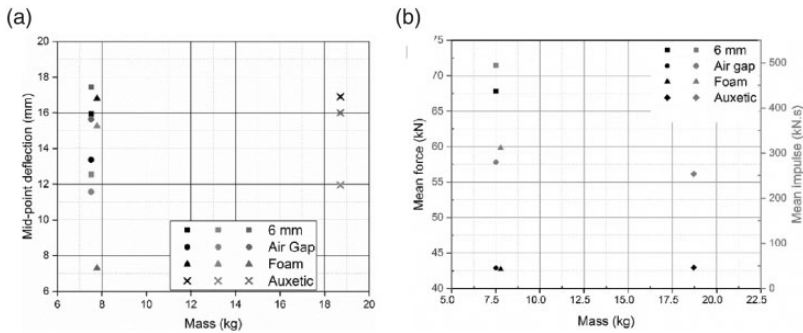
Figure 18. (a) Maximum deflection per panel type against mass; black = laser deflection, red = HSV deflection, blue = simulation deflection, (b) Mean force and mean impulse per panel type against mass.

Panel response with respect to panel mass

Figure 18 shows the plot comparison per panel against mass for maximum force, impulse and deflection. The mass of panel type were approximately 7.5 kg, 7.5 kg, 7.8 kg, and 18.7 kg for 6 mm panel, air filled, foam core and auxetic, respectively.

As presented in Figure 16(a)), comparison of each of the deflection measurements (i.e. laser system, HSV, and numerical modelling) found that foam panels were predicted to be the most effective, with the air filled experimental panels being the most efficient per unit mass. Alternatively the, auxetic core was comparable to the other systems in deflection behaviour but at a significant mass increase, making it an unfavourable strategy to deter the blast loading due to several reasons. Furthermore, Figure 16(b)) shows that the mean force and mean impulse against mass equal to the deflection response. The air filled panel could absorb the energy by deformed the face plate and reduced the received force and impulse in the back plate. By against it mass, the air filled panel is seen the most effective to deter 160 gram PE4 because due to the graph, that the response mean impulse and mean force of air filled panel placed in the most left and corner which means that the air filled is the least weight with the most effective in response. Contrary the auxetic core panel was under performed, even when normalized by the mass. The auxetic filled panel could absorb the impact energy and reduce the mean force and impulse, however by normalizing it by its mass makes the panel is heavier compared to the other panels.

Furthermore, we found the effect of sand humidity is not that sensitive in this study. As presented in Table 5 that the sand humidity recorded in the charge location of auxetic core panel test 4 is a slightly dense than other, approximately 46% below the PE4 charge, even the surrounding humidity is relatively similar for each test. The moister sand could not increase the explosion momentum. It is noticed that the recorded momentum in SX4 test and the other auxetic tested panels with lower

humidity are not far different. Rather, we presume that the momentum transfer mechanism through the panel core could determine the panel response.

In monolithic plates, the incoming shock wave imparts a velocity only to the face plate. The face plate is accelerated in responses to the impulse loading. The face plate would deform and vibrate to dissipate the energy. Meanwhile, in sandwich panels, the face panel would meet the core. The face panel immediately decelerated whilst the core and rear panel are accelerated. The energy lost is assumed as a dissipated energy due to the panel deformation or core compression [86]. In air filled panels the face plate would receive a transfer momentum from the shock wave of buried charge. The face plate would be displaced and deformed until 5 mm before contact with the back plate. The energy is dissipated as plastic deformation of face plate before impact the back plate. In foam filled panel, impact energy is dissipated into three components, i.e. face plate, solid foam, and back plate. Similarly with the foam filled, auxetic core panel will absorb the energy by three components, i.e. face plate, auxetic core, and back plate.

The authors are unclear why the sandwich panels do not exhibit the presumption performance. The relatively similar deflection could be caused by (i) the momentum transfer is insufficient to cause permanent displacement of the back plate and (ii) the layer at each panel behave independently because there is no bonding between them. Interestingly in [51], it was reported that there is a tendency with the 500 mm stand-off distance and 208 grams of TNT equivalent mass that the single panel is deflected relatively comparable with the sandwich configurations. This could be caused by the elastic behaviour of the panel. Moreover, related to the insufficient of loading impulse, the panel would displace independently instead of move together as a one sandwich panel as seen in Figure 19. In Figure 17(a), the trace of mid-point of monolithic is presented. The single point move freely, there is no momentum transfer, thus the panel would absorb the energy by a single plate. Meanwhile, Figure 17(b), c), d) shows a mid-point trace in the sandwich panels. In those panels, the momentum transfer occurred at the moment of impact between the layers. The air filled panels in Figure 17(b) shows a momentum transfer between the face and bottom plates. The face plate was plastically deformed until it reaches the bottom plate surface. It pushed the bottom plate and then the face plate was pushed back to forward direction and vibrated. In Figure 17(c) the trace of mid-point of foam filled panel was displayed. It can be observed that there is a delay between the first and the second momentum transfer. The first momentum transfer occurred at approximately 0.1 ms made the face plate and the top surface of the foam collided each other, while the second momentum occurred slightly after it at approximately 0.5 ms. Figure 17(d) shows the mid-point trace of auxetic core panels. The momentum transfer between the layers occurred almost at the same time, approximately at 0.45 ms. However, as stated before that it can be seen there is similarity mechanism between the sandwich panels that the plates of the panels deflected independently. At some time, the layers moved far apart at the momentum transfer. Meanwhile, at the other time they moved closer and impact occurred, the plates damped each other's movements.
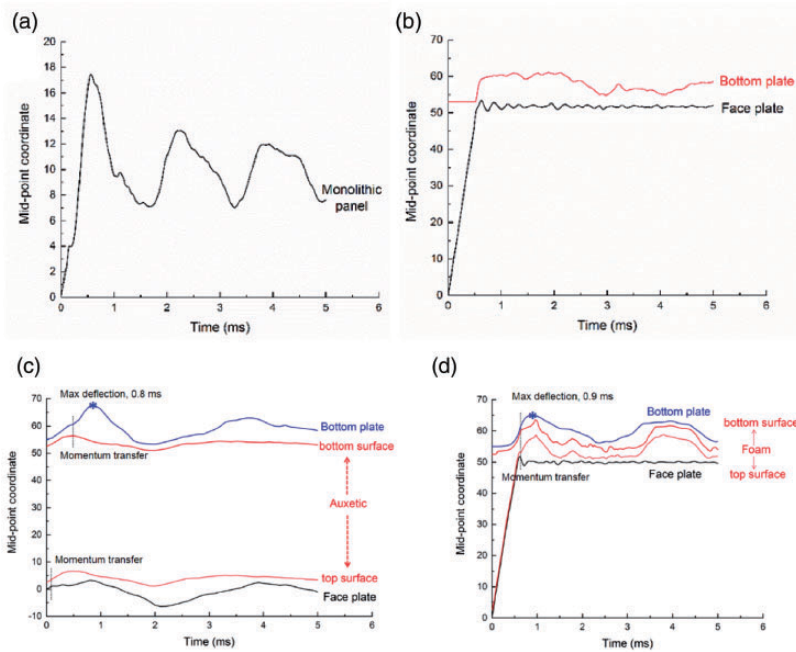
Figure 19. Mid-point momentum co-ordinate profile during explosion in transversal axis (z) for (a) monolithic, (b) air, (c) foam and (d) auxetic panels.

In auxetic core panels, at the time of momentum transferred the core plate would be accelerated and hit the back plate. At this stage, the core plate was decelerated and the back plate is accelerated. The plates behave independently because they are not tied by an adhesive or plastic deformation, thus the transferred momentum push the back plate and deflect it. It is possible to exhibit the comparable displacement between the auxetic and monolithic panel because the mass of back plate of auxetic panel is only 3 mm CR4 steel which is less than 6 mm monolithic panel (The 3 mm panel could have plastic deformation and hit the 50 mm back plate in air filled panel). Thus, the remaining energy of transferred momentum in back plate is still capable to deflect it until 11 to 16 mm.

In addition, it is also unclear that the dissipated energy of the compressed foam core could not damp the back plate in foam panels. We assume that the same transferred momentum mechanism occurred in the foam filled panels.

Conclusions

Auxetic and foam core panels are a promising structure against buried mines, as they demonstrated a lower loading response compared to the monolithic panels of the same material. Deflection measurements were highly variable throughout

testing, with the laser system reporting errors as great as 75%; a behaviour likely caused by its near location to the blast event. Nonetheless the air filled panels were the most promising at minimising rear plate deflection as confirmed by all three methods (HSV, laser system and computational modelling). Numerical modelling provided a good prediction of the plate deflections responses with some variation, which were likely caused by the simplified material models employed. Once normalised against panel weight, to understand how mass efficient each system was, the air filled panels were experimentally the most efficient per unit mass, with the auxetic core being the least effective.

Acknowledgement

Declaration of Conflicting Interests

The author(s) declared no potential conflicts of interest with respect to the research, authorship, and/or publication of this article.

Funding

ORCID iD

Faizal Arifurrahman (iD) https://orcid.org/0000-0003-3109-0187

References

1. Bird R. Protection of vehicles against landmines. *J Battlef Technol* 2001; 4: 14–17.
2. NATO (North Atlantic Treaty Organisation). *STANAG 4659: protection levels for occupant of armoured vehicles*. Washington: NATO, 2012.
3. NATO (North Atlantic Treaty Organisation). *AEP-55: procedures for evaluating the protection level of armoured vehicles – mine threat*. Washington: NATO, 2011.
4. Mann CT and Fischer H. *Recent trends in active-duty military deaths non-OCO deaths*, https://fas.org/sgp/crs/natsec/IF10899.pdf (accessed 30 October 2018).
5. Schneck W. *The development of mine resistant vehicles*. Virginia, USA: TARDEC, 1994.
6. Hazell PJ. *Armour: materials, theory, and design*. Boca Raton: CRC Press, 2016.
7. Yap CHK. The impact of armor on the design, utilization and survivability of ground vehicles: the history of armor development and use. Naval Postgrade School, Monterey California, 2012.
8. Donoghue JP, Alderson KL and Evans KE. The fracture toughness of composite laminates with a negative Poisson's ratio. *Phys Status Solidi B* 2009; 246: 2011–2017.

9. Qin H, Sun Y, Liu JZ, et al. Negative Poisson's ratio in rippled graphene. *Nanoscale* 2017; 9: 4135–4142.

10. Li T, Chen Y and Wang L. Enhanced fracture toughness in architected interpenetrating phase composites by 3D printing. *Compos Sci Technol* 2018; 167: 251–259.

11. McDonald SA, Dedreuil-Monet G, Yao YT, et al. In situ 3D X-ray microtomography study comparing auxetic and non-auxetic polymeric foams under tension. *Phys Status Solidi B* 2011; 248: 45–51.

12. Choi JB and Lakes RS. Nonlinear properties of polymer cellular materials with a negative Poisson's ratio. *J Mater Sci* 1992; 27: 4678–4648.

13. Jin S, Korkolis YP and Li Y. Shear resistance of an auxetic chiral mechanical metamaterial. *Int J Solids Struct* 2019; 174–175: 28–37.

14. Lorato A, Innocenti P, Scarpa F, et al. The transverse elastic properties of chiral honeycombs. *Compos Sci Technol* 2010; 70: 1057–1063.

15. Li D, Dong L and Lakes RS. The properties of copper foams with negative Poisson's ratio via resonant ultrasound spectroscopy. *Phys Status Solidi B* 2013; 250: 1983–1987.

16. Cheng H, Wang F, Bian Y, et al. Co- and self-activated synthesis of tailored multimodal porous carbons for solid-phase microextraction of chlorobenzenes and polychlorinated biphenyls. *J Chromatogr A* 2019; 1585: 1–9.

17. Chen CP and Lakes RS. Micromechanical analysis of dynamic behavior of conventional and negative Poisson's ratio foams. *J Eng Mater Technol* 1996; 288: 285–288.

18. Duc ND and Cong PH. Nonlinear dynamic response and vibration of sandwich composite plates with negative Poisson's ratio in auxetic honeycombs. *J Sandw Struct Mater* 2016; 20: 692–717.

19. Dinh N, Seung-Eock K, Hong P, et al. Dynamic response and vibration of composite double curved shallow shells with negative Poisson's ratio in auxetic honeycombs core layer on elastic foundations subjected to blast and damping loads. *Int J Mech Sci* 2017; 133: 504–512.

20. Critchley R, Corni I, Wharton JA, et al. A review of the manufacture, mechanical properties and potential applications of auxetic foams. *Phys Status Solidi B* 2013; 250: 1963–1982.

21. Alderson KL, Fitzgerald A and Evans KE. The strain dependent indentation resilience of auxetic microporous polyethylene. *J Mater Sci* 2000; 35: 4039–4047.

22. Argatov II, Guinovart-Díaz R and Sabina FJ. On local indentation and impact compliance of isotropic auxetic materials from the continuum mechanics viewpoint. *Int J Eng Sci* 2012; 54: 42–57.

23. Hu LL, Zhou MZ and Deng H. Dynamic indentation of auxetic and non-auxetic honeycombs under large deformation. *Compos Struct* 2019; 207: 323–330.

24. Dai Z, Weng C, Liu L, et al. Multifunctional polymer-based graphene foams with buckled structure and negative Poisson's. *Sci Rep* 2016; 6: 32989–32989.

25. Yu L, Yan Q and Ruzsinszky A. Negative Poisson's ratio in 1T-type crystalline two-dimensional transition metal dichalcogenides. *Nat Commun* 2017; 8: 15224–15228.

26. Lantada AD, De Blas Romero A, Schwentenwein M, et al. Lithography-based ceramic manufacture (LCM) of auxetic structures: present capabilities and challenges. *Smart Mater Struct* 2016; 25: 1–10.

27. Hou J, Deng B, Zhu H, et al. Magic auxeticity angle of graphene. *Carbon N Y* 2019; 149: 350–354.

28. Liu G, Zeng Q, Zhu P, et al. Negative Poisson's ratio in monolayer PdSe2. *Comput Mater Sci* 2019; 160: 309–314.
29. Zhang GH, Ghita O and Evans KE. The fabrication and mechanical properties of a novel 3-component auxetic structure for composites. *Compos Sci Technol* 2015; 117: 257–267.
30. Zhou L, Jiang L and Hu H. Auxetic composites made of 3D textile structure and polyurethane foam. *Phys Status Solidi B* 2016; 253: 1331–1341.
31. Alderson K, Nazaré S and Alderson A. Large-scale extrusion of auxetic polypropylene fibre. *Phys Status Solidi B* 2016; 253: 1279–1287.
32. Domaschke S, Morel A, Fortunato G, et al. Random auxetics from buckling fibre networks. *Nat Commun* 2019; 10: 1–8.
33. Jiang JW and Park HS. Negative Poisson's ratio in single-layer black phosphorus. *Nat Commun* 2014; 5: 1–7.
34. Dusfour G, LeFloc'h S, Cañadas P, et al. Heterogeneous mechanical hyperelastic behavior in the porcine annulus fibrosus explained by fiber orientation: an experimental and numerical approach. *J Mech Behav Biomed Mater* 2020; 104: 1–9.
35. Underhill RS. Defence applications of auxetic materials. *DSIAC J* 2014; 1: 7–13.
36. Sun Y, Xu W, Wei W, et al. Stab-resistance of auxetic weft-knitted fabric with kevlar fibers at quasi-static loading. *J Ind Text* 2019; 104: 1–13.
37. Novak N, Starčevič L, Vesenjak M, et al. Blast response study of the sandwich composite panels with 3D chiral auxetic core. *Compos Struct* 2019; 210: 167–178.
38. Imbalzano G, Linforth S, Ngo TD, et al. Blast resistance of auxetic and honeycomb sandwich panels: comparisons and parametric designs. *Compos Struct* 2018; 183: 242–261.
39. Qi C, Remennikov A, Pei LZ, et al. Impact and close-in blast response of auxetic honeycomb-cored sandwich panels: experimental tests and numerical simulations. *Compos Struct* 2017; 180: 161–178.
40. Imbalzano G, Tran P, Ngo TD, et al. Three-dimensional modelling of auxetic sandwich panels for localised impact resistance. *J Sandwich Struct Mater* 2017; 19: 291–316.
41. Imbalzano G, Tran P, Ngo TD, et al. A numerical study of auxetic composite panels under blast loadings. *Compos Struct* 2016; 135: 339–352.
42. Schenk M, Guest SD and McShane GJ. Novel stacked folded cores for blast-resistant sandwich beams. *Int J Solids Struct* 2014; 51: 4196–4214.
43. Jin X, Wang Z, Ning J, et al. Dynamic response of sandwich structures with graded auxetic honeycomb cores under blast loading. *Compos Part B Eng* 2016; 106: 206–217.
44. Bai X, Zhu L and Yu TX. Saturated impulse for pulse-loaded rectangular plates with various boundary conditions. *Thin-Walled Struct* 2017; 119: 166–177.
45. Cheng Y, Liu M, Zhang P, et al. The effects of foam filling on the dynamic response of metallic corrugated core sandwich panel under air blast loading – experimental investigations. *Int J Mech Sci* 2018; 145: 378–388.
46. Pardal G, Meco S, Dunn A, et al. Laser spot welding of laser textured steel to aluminium. *J Mater Process Technol* 2017; 241: 24–35.
47. Yuen SCK and Nurick GN. Experimental and numerical studies on the response of quadrangular stiffened plates. Part I: subjected to uniform blast load. *Int J Impact Eng* 2005; 31: 55–83.

48. Langdon GS, Yuen SCK and Nurick GN. Experimental and numerical studies on the response of quadrangular stiffened plates. Part II: localised blast loading. *Int J Impact Eng* 2005; 31: 85–111.

49. Pickering EG, Yuen SCK, Nurick GN, et al. The response of quadrangular plates to buried charges. *Int J Impact Eng* 2012; 49: 103–114.

50. Schwer L, Teng H and Souli M. LS-DYNA air blast techniques: Comparisons with experiments for close-in charges. In: *10th European LS-DYNA Conference 2015*. Würzburg, Germany. June 15–17, 2015.

51. Holloman RL, Deshpande V and Wadley HNG. Impulse transfer during sand impact with a cellular structure. *Int J Impact Eng* 2015; 82: 36–58.

52. Fleck NA and Deshpande VS. The resistance of Clamped sandwich beams to shock loading. *J Appl Mech* 71: 386–401.

53. Hutchinson JW and Xue Z. Metal sandwich plates optimized for pressure impulses. *Int J Mech Sci* 2005; 47: 545–569.

54. Tremblay JE and Delagrave R. *Impulse on blast deflectors from a landmine explosion*. Valcartier, Quebec: Defence Research Establishment, 1998.

55. Hallquist JO. *LS-DYNA theory manual*. Livermore, California: Livermore Software Technology Corporation. March, 2006.

56. Schwer L and Slavik T. Buried charge engineering model: Verification and validation. In: *9th European LS-DYNA Conference 2013*. Manchester, United Kingdom: DYNAore GmbH, p. 23.

57. LSTC. *LS-DYNA: keywors user's manual I*. Livermore: LSTC.

58. Bogosian D, Yokota M and Rigby S. TNT equivalence of C-4 and PE4: A review of traditional sources and recent data. In: *24th International Symposium on Military Aspects of Blast and Shock (MABS 24)*. Halifax, Canada: Springer Berlin Heidelberg. September 19–23, 2016. pp. 1–15.

59. Westin PS, Morris BL, Cox PA, et al. Development of computer program for floor plate response from land mine explosions. Technical Report No. 13045. US Army Tank-Automotive Command, Warren, MI, January, 1985.

60. Williams K, Mcclennan S, Durocher R, et al. Validation of a loading model for simulating blast mine effects on armoured vehicles. In: *7th International LS-DYNA Users Conference*, Detroit Michigan, USA. May 2002. pp. 35–44.

61. DoD. Structures to resist the effects of the accidental explosions. Washington D.C., USA. December 5, 2008.

62. Teich M and Gebbeken N. Structures subjected to low-level blast loads: analysis of aerodynamic damping and fluid-structure interaction. *J Struct Eng* 2012; 138: 625–635.

63. Librescu L, Oh S-Y and Hohe J. Linear and non-linear dynamic response of sandwich panels to blast loading. *Compos Part B Eng* 2004; 35: 673–683.

64. Hause T and Librescu L. Dynamic response of anisotropic sandwich flat panels to explosive pressure pulses. *Int J Impact Eng* 2005; 31: 607–628.

65. Hause T and Librescu L. Dynamic response of doubly-curved anisotropic sandwich panels impacted by blast loadings. *Int J Solids Struct* 2007; 44: 6678–6700.

66. Jones N. Strain rate behaviour of materials. In: *Structural impact*. Cambridge University Press, 1997, pp. 348–352.

67. Cowper GR and Symonds PS. Strain rate hardening and strain rate effects in the impact loading of cantilever beams. Armed Services Technical Information Agency, Office of Naval Research. Dayton, Ohio, 1957. pp. 40–45.

68. Wang ZL, Li YC and Wang JG. Numerical analysis of attenuation effect of EPS geofoam on stress-waves in civil defense engineering. *Geotext Geomembranes* 2006; 24: 265–273.

69. Chen W, Hao H, Hughes D, et al. Static and dynamic mechanical properties of expanded polystyrene. *Mater Des* 2015; 69: 170–180.

70. Overview of materials for low carbon steel. Material property data – matweb, www.matweb.com/search/DataSheet.aspx?MatGUID = 034970339dd14349a8297d2c 83134649 (accessed 24 October 2019).

71. Wickes DIY. Home improvement products for trade and DIY, www.wickes.co.uk/ (accessed 24 October 2019).

72. Panel Systems. Craftfoam blue for model making, product design & prototypes, www. panelsystems.co.uk/product/craftfoam-blue (accessed 7 January 2018).

73. AMETEK Material Analysis Division. Phantom Camera Control Help File. Vision Research. 2015.

74. Ramasamy A, Hill A, Hepper A, et al. Blast mines: Physics, injury mechanisms and vehicle protection. *J R Army Med Corps* 2009; 155: 258–264.

75. Bergeron DM and Tremblay JE. Canadian research to characterise mine blast output. In: *Proceedings of the 16th International Symposium on the Military Aspects of Blast and Shock*. Oxford, United Kingdom, 2000, pp. 501–511.

76. Deshpande VS, Mcmeeking RM, Wadley HNG, et al. Constitutive model for predicting dynamic interactions between soil ejecta and structural panels. *J Mech Phys Solids* 2009; 57: 1139–1164.

77. Børvik T, Olovsson L, Hanssen AG, et al. A discrete particle approach to simulate the combined effect of blast and sand impact loading of steel plates. *J Mech Phys Solids* 2011; 59: 940–958.

78. Rigby S, Fay SD, Tyas A, et al. Localised variations in reflected pressure from explosives buried in uniform and well-graded soils. In: *24th International Symposium on Military Aspects of Blast and Shock (MABS 24)*. Halifax, Canada: Springer Berlin Heidelberg. September 19-23, 2016. pp. 1–11.

79. Hlady SL, Bergeron D and Gonzalez R. Protecting vehicles from landmine blasts. In: *22nd International Symposium on Ballistics*. Vancouver, Canada, 2005, pp. 1239–1246.

80. Task Group TG-024. *Test Methodologies for Personal Protective Equipment Against Anti-Personnel Mine Blast*. Virginia, USA. March, 2004.

81. Bergeron D, Walker R and Coffey C. Detonation of 100-gram anti-personnel mine surrogate charges in sand: a test case for computer code validation. Suffield Report No. 668, DRES-SR-668, 1998.

82. Absil LHJ, Verbeek HJ, Weerheijm J. Combined experimental and numerical study of mine detonations in the vicinity of vehicles. In: *15th International Symposium on Military Aspects of Blast and Shock*. Banff, Alberta, Canada, September 14–19, 1997.

83. Gupta AD. Estimation of vehicle floor plate loading and response due to detonation of a mine shallow-buried in dry sand and wet tuff. In: *US Army ground vehicle survivability symposium*, Monterey, California USA. April 29–May 1, 1999.

84. Braid MP. Experimental investigation and analysis of the effects of anti-personnel land-mine blast effects, Suffield Report SSP 2001-188, 2001.
85. Hlady S. Effect of soil parameters on land mine blast. In: *18th Military Aspects of Blast and Shock (MABS)*. Bad Reichenhall, Germany, pp. 1–16.
86. Deshpande VS and Fleck NA. One-dimensional response of sandwich plates to underwater shock loading. *J Mech Phys Solids* 2005; 53: 2347–2383.

Appendix 1. Sand humidity

Table 5. Sand humidity around the charge, four points were measured around the charges and one point at the centre of the charge, respectively.

Test number	Testing code	Configuration	Sand humidity (%)
1	SS1	Single steel plate	14.6, 18.3, 16.7, 14.1, 18.7*
2	SS2	Single steel plate	12.3, 13.9, 12.3, 15.1, 12.8*
3	SS3	Single steel plate	13.8, 14.8, 14.6, 12.8, 12.3*
4	SS4	Single steel plate	16.1, 14.6, 18.7, 14.6, 16.6*
5	SA1	Steel - Air gap - Steel	13.5, 14.5, 14.6, 16.3, 14.6*
6	SA2	Steel - Air gap - Steel	14.1, 14.6, 15.6, 14.6, 13.4*
7	SA3	Steel - Air gap - Steel	14.1, 14.4, 13.8, 14.6, 15.7*
8	SF1	Steel - Styrofoam - Steel	14.6, 17.0, 19.5, 16.0, 14.6*
9	SF2	Steel - Styrofoam - Steel	20.3, 19.9, 20.7, 21.0, 14.6*
10	SF3	Steel - Styrofoam - Steel	16.2, 15.2, 16.9, 19.0, 16.7*
11	SX1	Steel - Auxetic core - Steel	19.1, 22.2, 20.8, 18.7, 21.8*
12	SX2	Steel - Auxetic core - Steel	20.5, 19.6, 22.3, 22.5, 23.6*
13	SX3	Steel - Auxetic core - Steel	14.1, 14.6, 16.0, 15.0, 16.8*
14	SX3	Steel - Auxetic core - Steel	12.8, 14.6, 19.1, 26.9, 46.8*